Article

Parkinson's disease gene, Synaptojanin1, dysregulates the surface maintenance of the dopamine transporter

Check for updates

Jacqueline Saenz [1,2], Elnaz Khezerlou[1], Meha Aggarwal[1], Amina Shaikh[1], Naga Ganti[1], Freja Herborg[3] & Ping-Yue Pan [1] ✉

Missense mutations of PARK20/*SYNJ1* (synaptojanin1/Synj1) were found in complex forms of familial Parkinsonism. However, the Synj1-regulated molecular and cellular changes associated with dopaminergic dysfunction remain unknown. We now report a fast depletion of evoked dopamine and impaired maintenance of the axonal dopamine transporter (DAT) in the *Synj1* haploinsufficient (*Synj1*+/−) neurons. While Synj1 has been traditionally known to facilitate the endocytosis of synaptic vesicles, we provide in vitro and in vivo evidence demonstrating that *Synj1* haploinsufficiency results in an increase of total DAT but a reduction of the surface DAT. *Synj1*+/− neurons exhibit maladaptive DAT trafficking, which could contribute to the altered DA release. We showed that the loss of surface DAT is associated with the impaired 5'-phosphatase activity and the hyperactive PI(4,5)P$_2$–PKCβ pathway downstream of Synj1 deficiency. Thus, our findings provided important mechanistic insight for Synj1-regulated DAT trafficking integral to dysfunctional DA signaling, which might be relevant to early Parkinsonism.

Mutations in the PARK20/h*SYNJ1* gene are linked to early onset Parkinsonism[1–8]. Our previous study further demonstrated reduced h*SYNJ1* transcripts in a subset of sporadic PD brains[9]. However, mechanisms underlying *SYNJ1*-associated Parkinsonian pathogenesis remain poorly understood. Synaptojanin1 (hSYNJ1/mSynj1), encoded by the *synj1* gene, is a lipid phosphatase that contains dual phosphatase domains and carboxy-terminal proline-rich domains. Over a dozen missense mutations or compound heterozygous mutations have been identified in the SAC1-like phosphatase, the 5'-phosphatase, and the proline-rich domains that are associated with Parkinsonism[8]. The phosphatase domains regulate the homeostasis of multiple species of phosphoinositides, including PI(3)P, PI(4)P, PI(3,5)P$_2$, PI(4,5)P$_2$, etc., and the proline-rich domain interacts with endocytic proteins, such as Endophilin A. Thus, Synj1 plays essential roles via its diverse domain functions in membrane trafficking[10–13]. Complete deletion of Synj1 is perinatally lethal. For almost three decades, Synj1 has been known to facilitate clathrin-mediated endocytosis of synaptic vesicles (SV)[14–19]. In Synj1-null neurons, an accumulation of clathrin-coated vesicles and pits was observed at the presynaptic terminal[10,19,20], and sustained neurotransmission was impaired[18,21]. Recent studies from us and others further suggested novel roles of Synj1 in autophagy[22–24]. Despite important

findings of Synj1 at fast-transmitting synapses and glial cells, its role in dysfunctional dopamine (DA) signaling in early Parkinsonian pathogenesis remains elusive.

To investigate the impact of Synj1 deficiency in the basal ganglia, our previous work showed that *Synj1* haploinsufficient (*Synj1*+/−) mice exhibited a reduction in striatal DA content and locomotor deficits at 12 months, which was followed by loss of dopaminergic (DAergic) terminals at 18 months[9]. We also demonstrated that synaptic vesicle (SV) recycling in the ventral midbrain (MB) neurons is more vulnerable to the *Synj1*+/− mutation than cortical neurons[9,25]. However, we found that the exocytosis kinetics was not impaired. In Parkinsonism-associated *SYNJ1* R258Q mutation knock-in (KI) mice, SV endocytosis was also impaired without affecting exocytosis[26]. More interestingly, large clusters of immunofluorescent dopamine transporter (DAT) were found in the dorsal striatum and these mice exhibit robust locomotor impairment at a young age (2–4 months)[26]. DAT is localized on the periphery of release sites of axonal membranes[27,28] to reuptake DA and terminate DAergic signaling[27–29]. Somatodendritic DAT also influences membrane excitability via its Na$^+$/Cl$^−$ symporter function[30,31]. The finding of abnormal DAT immunofluorescence in the KI mice suggested a possible role of Synj1 in regulating

[1]Department of Neuroscience and Cell Biology, Rutgers University Robert Wood Johnson Medical School, 675 Hoes Lane West, Piscataway, NJ, 08854, USA. [2]Rutgers Graduate School of Biomedical Sciences, Molecular Biosciences Graduate Program, 675 Hoes Lane West, Piscataway, NJ, 08854, USA. [3]Department of Neuroscience, University of Copenhagen, Blegdamsvej 3, DK-2200 Copenhagen, Denmark. ✉e-mail: pingyue.pan@rutgers.edu

DA signaling via pleiotropic mechanisms other than its well-known role in SV recycling. The potential influence of Synj1 on DAT may also be disease-relevant as disruptive mutations in DAT have been linked to both infantile and early onset Parkinsonism[32–35].

DAT recycles like most plasma membrane cargo. However, the molecular mechanisms mediating the recycling/internalization of DAT remain controversial. Both clathrin-dependent and independent endocytosis of DAT have been reported[36–45]. Our previous work suggested that Synj1 may participate in the cocaine-induced DAT trafficking[46], however, whether Synj1 regulates DAT recycling in physiological conditions has not been explored. Neither do we understand the interactions between DA signaling and DAT surface availability in Synj1-deficient conditions. We now use a combination of sophisticated imaging tools, including dLight[47,48], DAT-pHluorin[46], and a fluorescent DAT ligand[45] to dissect Synj1's impact on DA homeostasis and the surface maintenance of DAT. Our results revealed an unexpected role of Synj1's 5'-phosphatase domain in maintaining the surface maintenance of DAT by suppressing the PI(4,5)P$_2$–PKCβ pathway, and we provided essential insights for dysregulation of DA signaling via the dynamic availability of DAT.

Results

The evoked DA release and basal DA level are altered in *Synj1*+/− neurons

Our previous study of the *Synj1*+/− mice suggested an age-dependent decline of striatal DA metabolism[9]. To further assess how Synj1 regulates DA homeostasis, we sought to measure evoked DA transients using recently developed dLight1.3b DA sniffer cells[47]. Following an initial validation for the dose–responses (Supplementary Fig. 1a–c), we generated ventral MB-sniffer cell coculture (see the "Methods" section, Fig. 1a), which have been shown previously to detect basal and amphetamine-induced DA release[49,50]. We verified the stimulation-dependent DA release from DAergic axons grown beneath the sniffer cells (Fig. 1a, b), suggesting the sensitivity and reliability of DA sensing. In littermate *Synj1*+/+ and *Synj1*+/− cocultures, we measured dLight-DA transients in response to various lengths (1, 2.5, and 10 s) of field electrical stimulation at 20 Hz (Fig. 1c, d). The amplitude of dLight transients was not different between *Synj1*+/+ and *Synj1*+/− neurons at all stimulations (Fig. 1e). Recognizing this measure might be affected by variable DAergic axons being sampled, we performed post hoc analysis of release per length of tyrosine hydroxylase (TH)-positive axons. This analysis again failed to identify a difference between *Synj1*+/+ and *Synj1*+/− neurons (Supplementary Fig. 2). We then assessed the kinetics of dLight responses by rescaling the fluorescence at the stimulation endpoint to 1. The *Synj1*+/− neurons took a significantly shorter time to reach peak response at moderate (2.5 s) to long (10 s) stimulations (Fig. 1f). We then evaluated the decline phase of the dLight response, which is indicative of DA clearance. The decay time constant was not significantly altered in *Synj1*+/− neurons (Fig. 1g). However, the dLight fluorescence exhibited abnormal decline below the baseline following short (1 s) to moderate (2.5 s) stimulations (Fig. 1h) in mutant neurons.

To determine whether the abnormal DA clearance results in reduced extracellular DA, we measured basal DA level in cultured littermate neurons using a different sniffer cell line, GRAB$_{DA1H}$, with slow binding and nanomolar DA sensitivity (Supplementary Fig. 1c, d)[47]. Using the similar cocultures system as introduced above, we performed a random sampling of the sniffer cell basal fluorescence using consistent imaging settings. Surprisingly, the GRAB$_{DA1H}$ fluorescence was increased in *Synj1*+/− cultures compared to littermate *Synj1*+/+ cultures (Fig. 1i-j) despite similar densities of dopaminergic neurites in post hoc analysis (Fig. 1k). Thus, our data suggested abnormality in the kinetics of evoked DA release and enhanced basal DA signaling in *Synj1*+/− neurons.

Increased DAT expression in *Synj1*+/− brains and neurons

Recent studies suggested that Synj1 may regulate DAT expression and function[26]. We thus wondered if the altered DA dynamics in *Synj1*+/− neurons could be due to changes in DAT, especially as our previous study

found a lack of evidence for SV exocytosis[25]. We first examined the overall expression of DAT in *Synj1*+/+ and *Synj1*+/− mice. We performed immunofluorescence analysis of DAT in *Synj1*+/+ and *Synj1*+/− littermate mice containing both sexes ($n = 6$ males, $n = 4$ females in each genotype) at 12–18 months. An earlier study of the *SYNJ1* R258Q knock-in (KI) mouse found large clusters of immunoreactive structures of DAT in the dorsal but not the ventral striatum[26]. In *Synj1*+/− mice, we did not observe similar DAT clusters in either the dorsal or ventral striatum, however, we observed an overall increase in DAT optical density, which is more robust in the male mice (Fig. 2a, b). In a separate approach, we used western blotting to analyze DAT levels in *Synj1*+/+ and *Synj1*+/− littermate mice ($n = 8$ males, $n = 4$ females in each genotype, 10–12 months). Consistently, we observed a male-specific increase in DAT. The increased DAT was found in both triton soluble and insoluble fractions of the MB samples, but specifically enriched in the triton-insoluble fractions of striatal samples of the *Synj1*+/− brains (Supplementary Fig. 3), suggesting different processing of the endocytic DAT in the soma and axons of the *Synj1*+/− mice.

The sex differences in DAT function have been documented for over a decade[51–53]. To determine if the changes in DAT level can be captured in cultured DA neurons prepared from pups of both sexes, we conducted immunofluorescence analysis. Our analysis demonstrated that total DAT expression at the soma and axons was increased in tyrosine hydroxylase (TH) positive neurons (Fig. 2c–e).

Synj1+/− mice exhibit decreased surface DAT in the axons

DAT is recycled in a regulated manner. To determine if Synj1 regulates surface DAT abundance, we incubated live MB neurons with a fluorescent cocaine analog, JHC1-64[54], which has been shown in many recent studies to reveal the surface availability of DAT[55,56]. The specificity of the JHC analysis was verified by the lack of staining in the presence of a DAT blocker, cocaine (Fig. 3a). Live JHC dye staining showed reduced surface DAT (sDAT) in the axons of *Synj1*+/− neurons without a significant change at the soma (Fig. 3b). In a separate approach, we expressed a pH-sensitive DAT sensor, CAGp-hDAT-pHluorin[46] in cultured ventral MB neurons. Sequential perfusion of a membrane-impermeable MES solution (pH 5.5) and a pH-neutral NH$_4$Cl solution (pH 7.4) (Fig. 3c) allowed us to calculate the surface fraction and vesicular pH of the intracellular DAT-pHluorin using the Henderson–Hasselbalch equation[46,57–59]. The TH immunoreactivity of the neuron was determined by *post hoc* analysis (raw data in Supplementary Fig. 4). Data from both TH+ and TH− neurons were combined in Fig. 3d, e, which indicated that the *Synj1*+/− mutation reduces surface DAT fraction in the neuronal axons (Fig. 3d). The acidity of intracellular DAT vesicles was not different in the axons; however, it was reduced at the soma (Fig. 3e), suggesting their possible degradative fate.

To further verify that Synj1 deficiency downregulates the surface expression and function of DAT in vivo, we performed a locomotor behavioral analysis of intraperitoneal (i.p.) injection of a DAT agonist, amphetamine (AMPH). Transgenic mice with 2–3-fold DAT over-expression and a 30% increase in surface DAT exhibited enhanced AMPH-induced locomotion[60]. On the other hand, reduced psychomotor functions are often reflective of a lack of functional DAT[61]. We examined a young cohort (3–6 months, $n = 8$ males and $n = 8$ females in each genotype) and an old cohort (12–18 months, $n = 7$ males and $n = 8$ females in the *Synj1*+/+ group; $n = 7$ males and $n = 6$ females in the *Synj1*+/− group) of littermate *Synj1*+/− and *Synj1*+/+ mice containing both male and females (Fig. 3f, g). In agreement with our ex vivo DAT analysis (Fig. 2a, b, Supplementary Fig. 3), reduced psychomotor activity was only observed in the male *Synj1*+/− mice (Fig. 3f, g, left panels) but not the female *Synj1*+/− mice (Fig. 3f, g, right panels), and this defect remains consistent across two age groups.

Synj1+/− neurons exhibit impaired DAT trafficking in response to dopamine

The increased overall DAT expression and reduced surface availability of DAT in *Synj1*+/− axons indicated a defect in DAT trafficking at basal
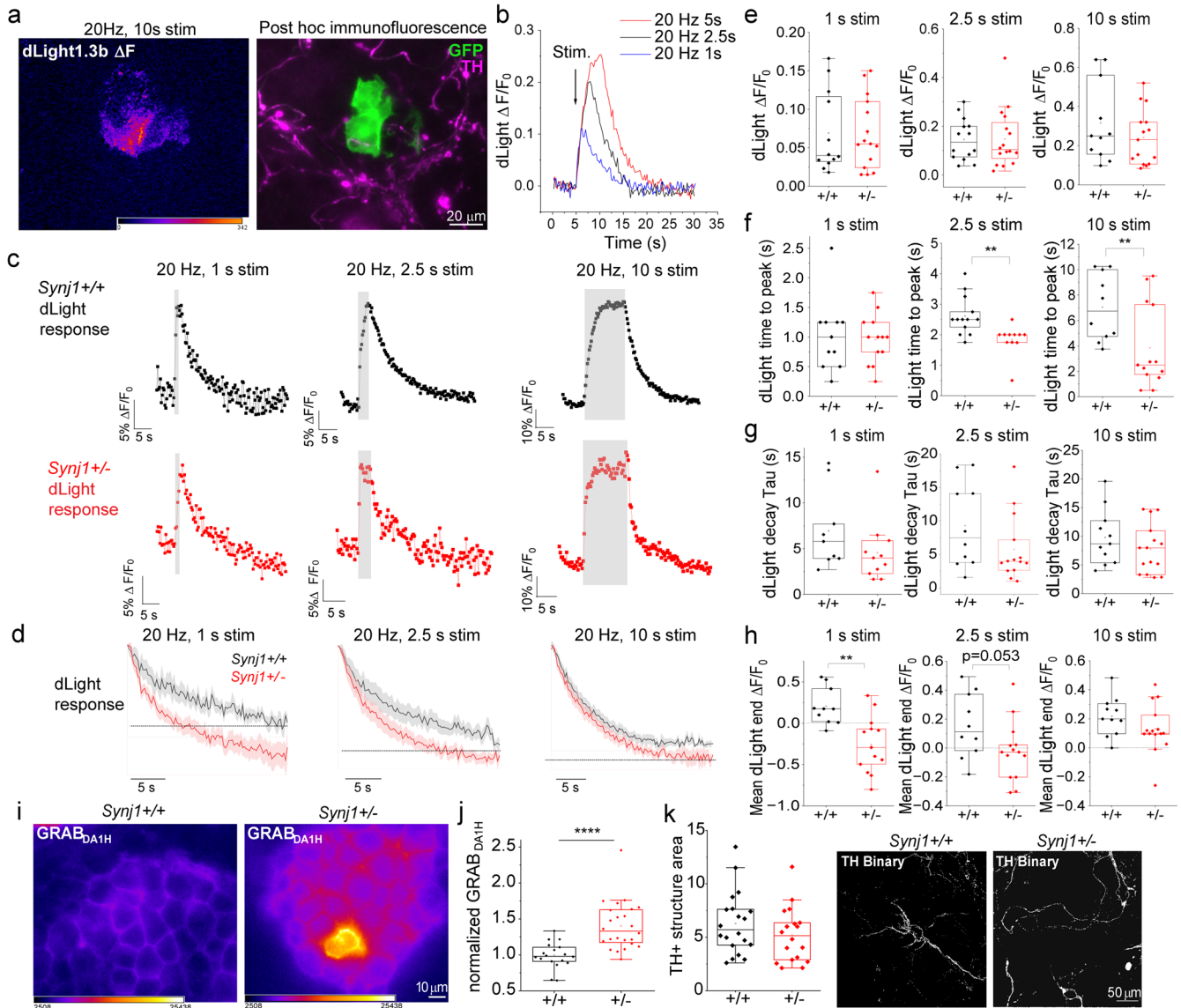
Fig. 1 | The evoked DA release and basal DA level are altered in the *Synj1+/−* neurons. a Representative dLight1.3b sniffer cell response to a 20 Hz, 10 s field stimulation on a heatmap scale (left). Post hoc Immunolabeling of tyrosine hydroxylase (TH) and GFP determines the specificity of dLight response from proximal DAergic axons (right). Peripheral DAergic axons do not contribute significantly to the dLight response (data not shown). **b** Background subtracted $\Delta F/F_0$ dLight traces to sequential stimulations at 20 Hz from a representative neuron. **c** Representative $\Delta F/F_0$ dLight traces from *Synj1+/+* and *Synj1+/−* littermate cultures at different stimulation lengths. **d** The $\Delta F/F_0$ dLight responses were normalized to the fluorescence at the end of stimulation and aligned to compare the decay curve (mean ± SEM) relative to baseline (F_0, dotted line) for *Synj1+/+* and *Synj1+/−* neurons at 20 Hz, 1 s (left), 2.5 s (middle) and 10 s (right) stimulations.

e–h Summarized $\Delta F/F_0$ peak response (**e**), time to peak (**f**), decay time constant (**g**), and $\Delta F/F_0$ end fluorescence (**h**) in *Synj1+/+* and *Synj1+/−* neurons from littermate cultures. ******$p < 0.01$, Mann–Whitney test or Student's *t*-test. Data from five batches of cultures. **i** Representative basal GRAB$_{DA1H}$ fluorescence on a heatmap scale from littermate MB-sniffer cell cocultures. **j** Normalized GRAB$_{DA1H}$ fluorescence from three batches of littermate cultures. ********$p < 0.00001$, Student's *t*-test. **k** Analysis of DAergic axons in the *Synj1+/+* or *Synj1+/−* cultures. Each data point is the analysis of one large view image (represented in the right panel). ≥3 fields were analyzed for each culture for a total of five batches of cultures. TH immunofluorescence was transformed into a binary image after background subtraction to calculate the TH axon area (right panels).

conditions. Our previous study using DAT-pHuorin suggested aberrant DAT insertion following cocaine exposure in *Synj1+/−* axons[46]. Nonetheless, cocaine is not a physiological ligand of DAT. To investigate the endogenous mechanisms that may be responsible for intracellular DAT retention, we examined DAT trafficking in response to DA. Cultured midbrain neurons were transfected with DAT-pHluorin to reveal the DAT trafficking dynamics in neurites (Fig. 4a). A 3-min perfusion of 10 μM DA hydrochloride in cultured *Synj1+/+* MB neurons led to an average increase in DAT-pHluorin fluorescence at the soma (Fig. 4b–d, Supplementary Fig. 5a). In contrast, *Synj1+/−* neuronal soma exhibited fluorescence reduction (Fig. 4c, d, Supplementary Fig. 5a). In the axons, a fluorescence increase was

also observed in *Synj1+/+* neurons during the perfusion of DA followed by a sharp decline (Fig. 4f, g, Supplementary Fig. 5b). In contrast, the *Synj1+/−* axons exhibited a progressive loss of DAT-pHluorin fluorescence following a steady baseline (Fig. 4g, h, Supplementary Fig. 5b), indicating DAT internalization. We analyzed the slope of fluorescence decline from the positive peak to the negative peak in *Synj1+/+* axons and used the same time window to fit the decay slope in Synj1+/− axons. We found a steeper decline in *Synj1+/+* axons compared to the Synj1+/− axons (Fig. 4i). The slower fluorescence decline is consistent with the role of Synj1 in assisting vesicular endocytosis. Importantly, our data suggests that this well-known role of Synj1 may only be engaged following DAT exocytosis. The steeper

**Fig. 2 | Increased DAT expression in *Synj1*+/−
neurons. a** Representative coronal striatal slices
from a *Synj1*+/+ mouse and a *Synj1*+/− mouse
immunolabeled for Synj1 (red) and DAT (blue).
Confocal images were captured using a lower and a
higher magnification objective and presented in
different scales. **b** Analysis of the optical density of
DAT immunofluorescence at high magnification in
the striatum from *Synj1*+/+ ($n = 6$ males $+ 4$
females) and *Synj1*+/− ($n = 6$ males $+ 4$ females)
mice at 12–18 months. Each data point is an average
value from one mouse. *$p = 0.024$, Student's *t*-test
with Welch correction for unequal variance.
c Representative immunofluorescence images of
cultured ventral midbrain neurons immunolabeled
with anti-TH (green) and anti-DAT (red). White
and blue boxed regions are axons and soma,
respectively, which are magnified on the right
panels. **d** and **e** Normalized immunofluorescence of
DAT in the axons (**d**, by line selection) and soma
(**e**, by area selection) of *Synj1*+/+ and *Synj1*+/− DA
neurons. *$p < 0.05$, ****$p < 0.0001$. Mann–Whitney
tests. Data from 2 to 3 batches of cultures.
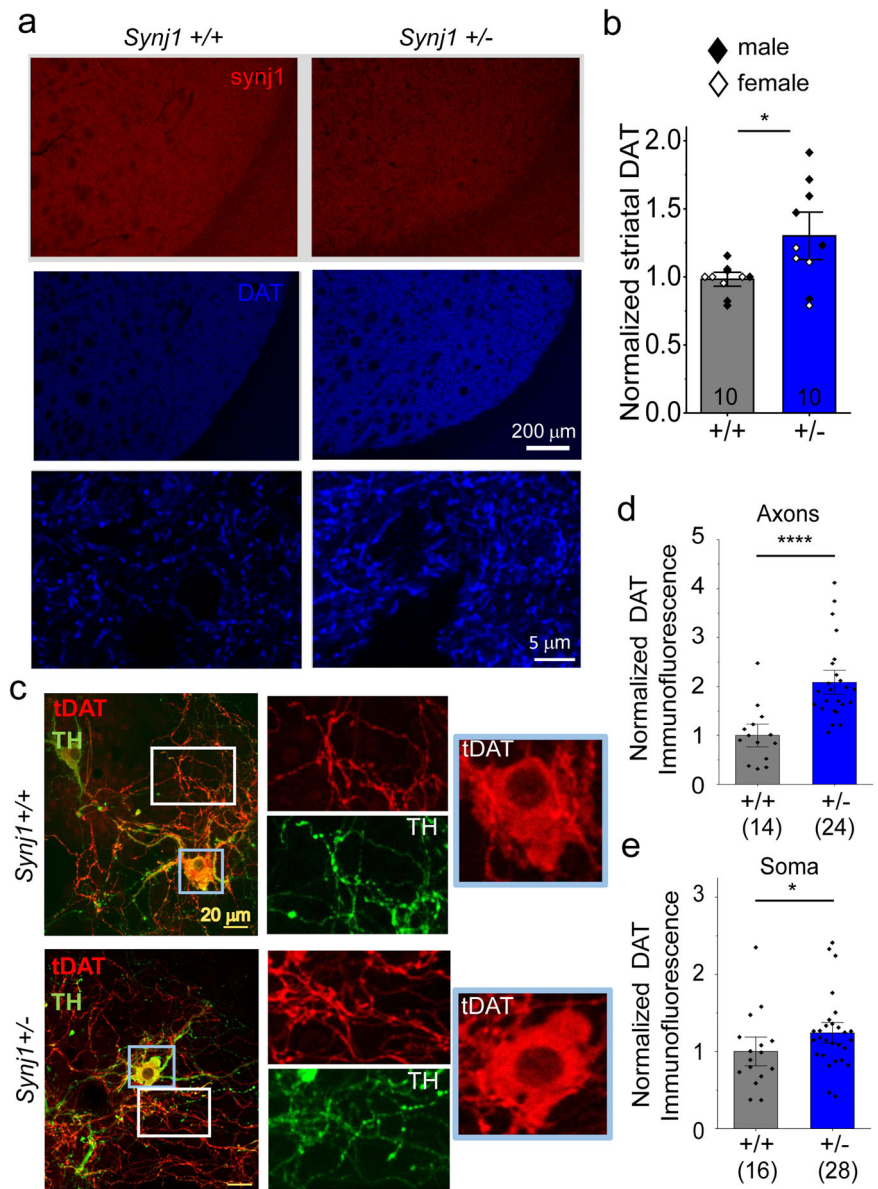
endocytosis of DAT following a brief DA exposure in wild-type neurons
may represent an adaptive response to maintain the homeostasis of the
extracellular DA level. The lack of adaptive DAT trafficking in *Synj1*+/−
neurons may contribute to the accelerated DA peak time and abnormal
clearance measured by dLight (Fig. 1d, h).

**The number of large varicosity is not altered in cultured *Synj1*+/−
neurons**
Over a dozen mutations have been identified in the human *SYNJ1* coding
region that is associated with complex Parkinsonism[8], but only one *SYNJ1*-
PD model, the R258Q KI mouse, has been characterized[26]. A striking finding
from the R258Q KI mice was the presence of large DAT clusters[26], which
was more widespread in a double mutant mouse with simultaneous deletion
of PARK19/Auxilin[62,63]. Given the PD-like motor deficits and pathology in
the aged *Synj1*+/− mice[9], we sought to determine whether they share
similar DAT pathology as the KI mice. While we did not observe DAT
clusters in the brain slices of *Synj1*+/− mice, large varicosities are not
uncommon in cultured ventral MB neurons. In our previous study, we
showed that large varicosities exhibit 25% of sDAT compared to adjacent
axons that exhibit 75% in wild-type neurons[46]. We next sought to determine

if the reduced axonal sDAT could be due to a higher density of large
varicosities in the *Synj1*+/− axons. In cultured *Synj1*+/+ and *Synj1*+/−
neurons expressing DAT-pHluorin, we immunolabeled with anti-GFP for
DAT, anti-TH for DAergic axons, and anti-synapsin1/2 for release sites (Fig.
5a). Large varicosities were defined by their size, which segregated from
synapsin positive boutons (Fig. 5b, see the "Methods" section). These large
varicosities also exhibited significantly lower and diffused staining for
synapsin1/2 (Fig. 5a, c), which distinguished them from boutons. Com-
paring *Synj1*+/+ and *Synj1*+/− axons from three batches of cultures, we
did not observe any difference in the density of large varicosities (Fig. 5d),
suggesting that dystrophic changes in DAT may not be a key pathogenic
characteristic of the *Synj1*+/− mice.

**Synj1's 5'-phosphatase domain is essential for the maintenance
of sDAT expression**
To investigate the Synj1 downstream signaling mechanisms contributing to
the reduced sDAT in *Synj1*+/− neurons, we expressed human SYNJ1
cDNAs containing previously characterized functional mutations in the
N2a cells to assess the sDAT abundance. The R258Q mutation (R > Q
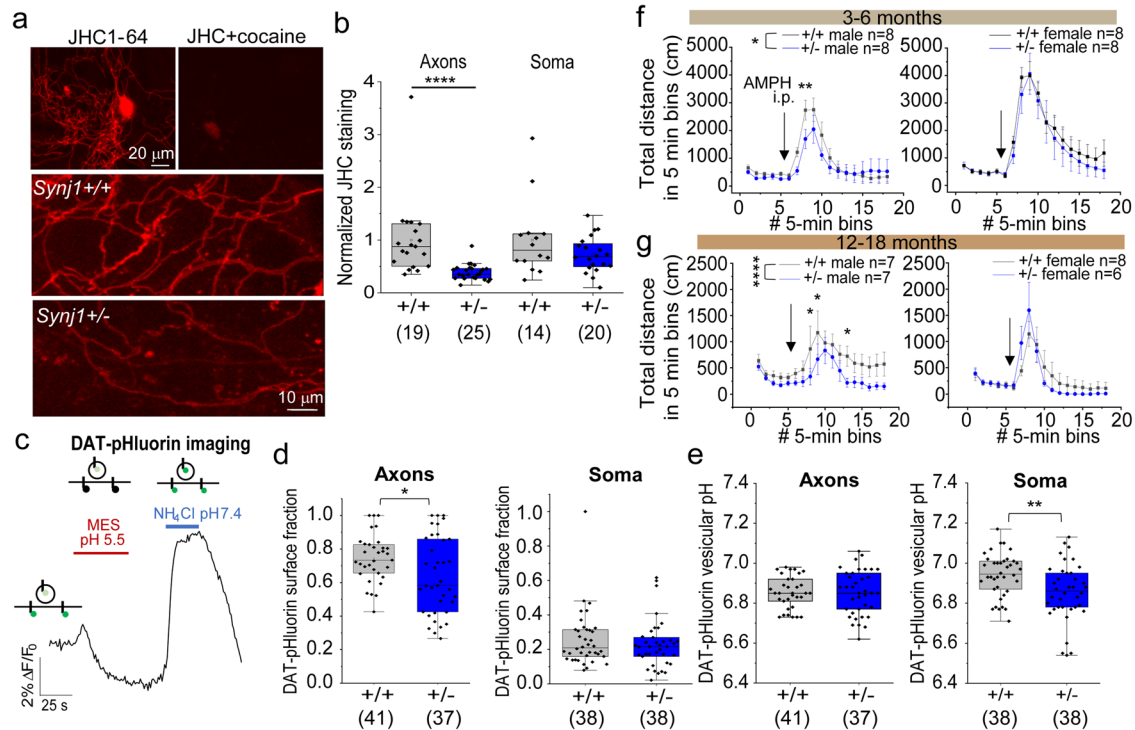mutant) abolishes the PI(3)P and PI(4)P hydrolysis activities of the SAC1

Fig. 3 | *Synj1*+/− neurons exhibit decreased surface DAT expression and function. a Top, representative images of MB culture live stained with a fluorescent cocaine analog JHC1-64, which was blocked in the presence of 10 μM cocaine. Bottom, representative images of JHC staining in *Synj1*+/+ and *Synj1*+/− cultures. **b** Normalized fluorescence of JHC1-64 at the axons (by line selection) and the soma (by area selection). ****$p < 0.0001$. Mann–Whitney test. Data from 2 to 3 batches of cultures. **c** Representative DAT-pHluorin trace to sequential perfusion of a membrane-impermeable MES acid solution and a pH 7.4 NH₄Cl solution. Insets, illustration of DAT-pHluorin fluorescence change during the perfusion of the two distinct pH solutions. **d** and **e** Box plots summarizing the surface fraction (**d**) and vesicular pH (**e**) of DAT-pHluorin in the neuronal axons and soma calculated using

the Henderson–Hasselbalch equation. *$p < 0.05$, **$p < 0.01$, Student's *t*-test. **f** and **g** Amphetamine-induced locomotor activity was analyzed in a young cohort (3–6 months, **f**) and an old cohort (12–18 months, **g**) littermate mice using the open-field assay. Male and female mice were plotted separately due to sex-segregated responses to amphetamine in the *Synj1*+/− mice. Two-way ANOVA, $p < 0.0001$ for a time in all groups. *$p = 0.025$ for genotype in the young male cohort (**f**, left). $p = 0.14$ for the genotype in the young female cohort (**f**, right). ****$p < 0.0001$ for genotype in the old male cohort (**g**, left), $p = 0.58$ for genotype in the old female cohort. Arrow indicates the time of amphetamine 5 mg/kg i.p. injection. Asterisk on trace were *$p < 0.05$, **$p < 0.01$ from Tukey's multiple comparison test.

enzyme without affecting the 5'-phosphase (5'-PPase) activity, whereas, the R839C mutation (R > C mutant) reduces both phosphatases[9]. The D769A mutation (D > A mutant) completely abolishes the 5'-PPase activity to hydrolyze PI(4,5)P₂[15] and was also included in this analysis (Fig. 6a, b). The MES and NH₄Cl solutions were perfused, as shown earlier (Fig. 3c) to measure the surface fraction of DAT-pHluorin and its vesicular pH. Consistent with the role of Synj1 in maintaining sDAT, we found that WT SYNJ1 expression led to an increase in sDAT and significantly more alkaline DAT-containing vesicles. Among all mutations, N2a cells expressing the SYNJ1 R > C mutation exhibited the most significant impairment in sDAT fraction and more acidic DAT vesicles compared to WT SYNJ1 expressing cells (Fig. 6c, d). The SYNJ1 D > A mutant expressing cells also exhibited a lower surface fraction and more acidic DAT-vesicles (Fig. 6c, d). We did not observe a significant reduction in the DAT surface fraction in SYNJ1 R > Q expressing cells; however, the DAT-vesicles were significantly more acidic than those in WT SYNJ1 expressing cells (Fig. 6c, d). Taken together, these results suggested that both enzymatic domains of Synj1 regulate DAT trafficking, albeit in slightly distinct manners.

To account for the possibility of differential expression among WT and mutant SYNJ1 cDNAs, we conducted a different set of experiments that co-expressed an N-terminally tagged RFP-DAT with different eGFP-tagged SYNJ1 variants (Fig. 6). We measured the surface to intracellular DAT (sDAT/iDAT) fluorescence in live N2a cells exhibiting eGFP fluorescence and plotted their sDAT/iDAT values against normalized eGFP-SYNJ1 levels. In agreement with the DAT-pHluorin analysis, while no significant difference was observed for the exogenously expressed SYNJ1 level across all

groups, the R > C and D > A mutant expressing cells exhibited significantly lower sDAT/iDAT compared to that from the WT SYNJ1 cells (Fig. 6f). The R > Q mutant was again no different than the WT SYNJ1, further suggesting that the 5'-PPase is essential in maintaining the balanced distribution of sDAT at baseline.

The axonal sDAT is regulated by Synj1 via the PI(4,5)P₂-PKCβ pathway

To further investigate the impact of Synj1's 5'-PPase and its main enzymatic substrate, PI(4,5)P₂, on DAT trafficking, we sought to transiently increase the plasma membrane PI(4,5)P₂ and examine the dynamic change of sDAT. In our previous study using antibody labeling of endogenous DAT, we showed that inhibiting phosphoinositide 3-kinases (PI3K) with a pharmacological agent, LY294002 (LY) (Fig. 7a), effectively mimicked Synj1 deficiency by increasing plasma membrane PI(4,5)P₂ at neuronal soma[9]. To observe the simultaneous change in PI(4,5)P₂ level and DAT trafficking, we co-expressed a red-shifted PI(4,5)P₂ biosensor, RFP-PH-PLCδ and DAT-pHluorin in cultured WT ventral MB neurons (Fig. 7b) and performed dual-channel live cell imaging. Perfusion of 100 μM LY led to an increase in the RFP fluorescence at both neuronal soma (Fig. 7c) and axons (Fig. 7d) within a minute, suggesting an increase in PI(4,5)P₂. The DAT-pHluorin fluorescence started to decline with a brief delay following the peak RFP fluorescence, suggesting DAT internalization. Consistently, we observed reduced surface YFP-DAT in N2a cells after a 10-min treatment of 100 μM LY (Fig. 7e), further suggesting that increasing plasma membrane PI(4,5)P₂ induces DAT internalization.
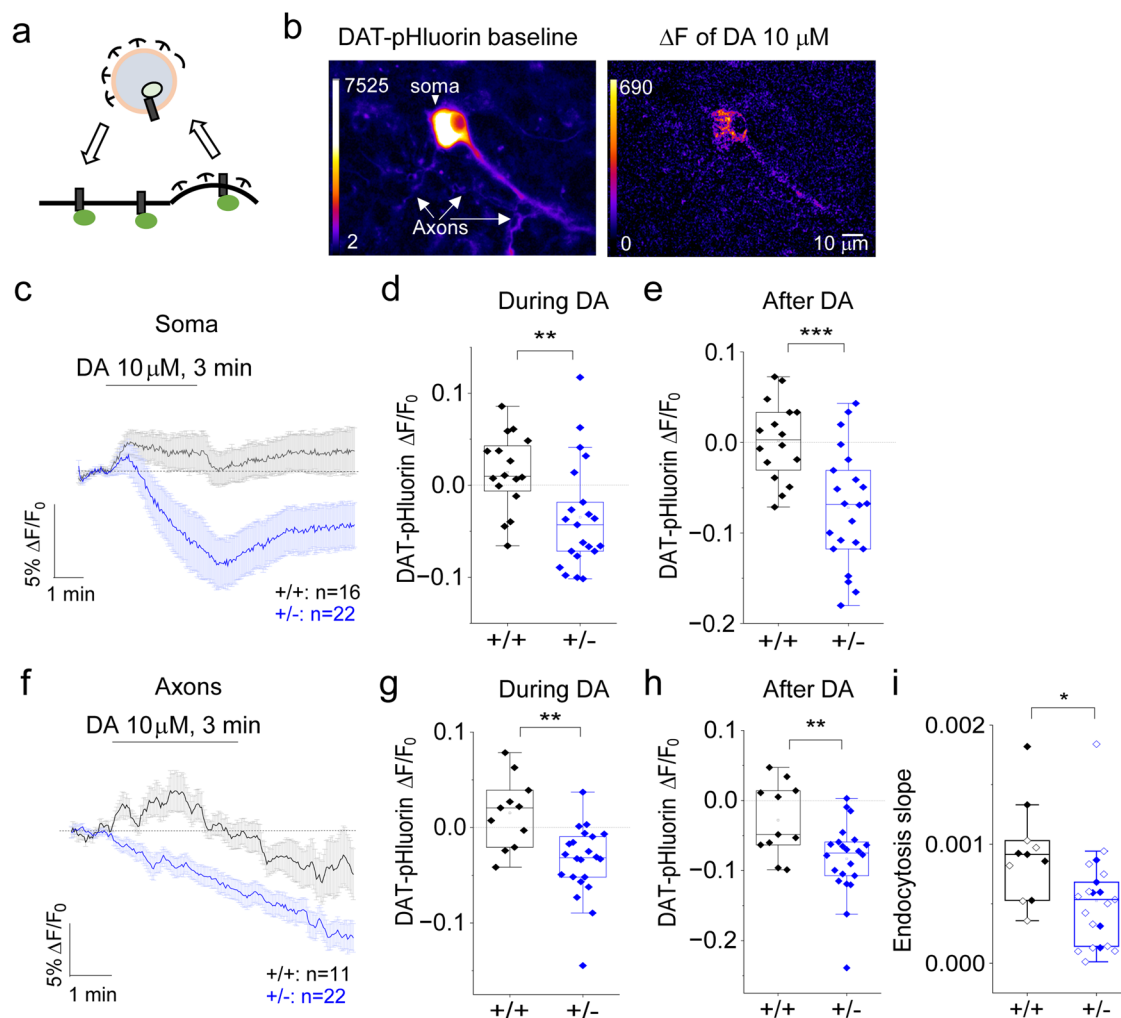
Fig. 4 | *Synj1*+/− neurons exhibit enhanced DAT internalization in response to DA. a Working model of DAT-pHluorin fluorescence change during exocytosis and endocytosis. **b** Representative ventral MB neuron expressing DAT-pHluorin at baseline (left) and the fluorescence change (ΔF) in response to perfusion of a 10 μM DA solution (right). The fluorescence was presented using a heat scale. **c** and **f** The average soma (**c**) and axon (**f**) DAT-pHluorin response to 3-min perfusion of 10 μM DA from *Synj1*+/+ and *Synj1*+/− neurons. Data were represented as mean ± SEM. **d** and **e** Summary of the averaged soma DAT-pHluorin response during the 3-min DA perfusion (**d**) and within 1.5 min after the DA perfusion (**e**). **g** and **h** Summary of the averaged axonal DAT-pHluorin response during the 3-min DA perfusion (**g**) and within 1.5 min after the DA perfusion (**h**). *******p* < 0. 01, Student's *t*-test. **i** Comparison of the linear fit slope of the DAT-pHluorin fluorescence decline. Fitting windows for all neurons were from 2 min 40 s (positive peak in *Synj1*+/+ neurons) to 5 min (negative peak in *Synj1*+/+ neurons). Solid symbols are TH+ neurons, and open symbols are TH− neurons determined by post hoc immunofluorescence. *p < 0.05, Student's *t*-test.

The above RFP-PH-PLC$_\delta$ experiment also suggested that increased PI(4,5)P$_2$ in *Synj1*+/− neurons could result in the recruitment of phospholipase C (PLC) to produce IP3 and diacylglycerol (DAG), important co-factors that regulate the activation of a large family of protein kinase C (PKC)[64,65]. PKC has been shown to phosphorylate DAT and induce its internalization[41,43,66–68]. We wondered if Synj1 regulates neuronal DAT maintenance via PKC signaling. Different PKC isoforms may be enriched in specific cell types and even distinct subcellular compartments to be in close proximity to their activators and substrates[65]. Among all PKC isoforms, we specifically examined PKCα and PKCβ, which contain a C2 domain that directly binds PI(4,5)P$_2$[64]. Our immunofluorescence analysis suggested that PKCα expression was only found in 73% of TH+ neuronal soma (out of *n* = 41, from 2 batches of cultures) and majority of TH+ axons were devoid of PKCα staining (Supplementary Fig. 6a). Instead, PKCβii immunofluorescence was present in 96% out of *n* = 23 TH+ neuronal soma with evident expression in the TH+ axons as well (Supplementary Fig. 6b). We did not observe an increased expression of PKCβii in *Synj1*+/− neurons (Supplementary Fig. 6c, d). To assess the possibility of enhanced PKCβii activity in *Synj1*+/− neurons, we performed a western blot analysis of the striatal tissues using a phosphor-specific antibody targeting PKCβii-Ser660[69]. Consistent with previous in vivo (Fig. 3f, g) and ex vivo (Fig. 2a, b, Supplementary Fig. 3) analyses, we found increased pSer660 PKCβ in the male, but not female *Synj1*+/− mice (Supplementary Fig. 7). To further verify the enhanced PKCβ activity is responsible for reduced sDAT in *Synj1*+/− neurons, we transfected DAT-pHluorin with an shRNA targeting mouse PKCβ (Fig. 8a, b). This strategy led to a 75-80% knockdown (KD) of the PKCβii. The sequential perfusion of MES and NH₄Cl solutions revealed an effective reversal of sDAT fraction in the axons but not at the soma (Fig. 8c). In a parallel study, we treated ventral MB neurons with a PKCβ specific inhibitor, Ruboxistaurin (Rubo, 1 μM), overnight before assessing the sDAT in *Synj1*+/+ and *Synj1*+/− neurons. We found that while Rubo did not affect the sDAT in *Synj1*+/+ neurons, it effectively reversed the sDAT fraction in *Synj1*+/− neurons at both

Fig. 5 | The density of axonal varicosities is not altered in _Synj1_+/− neurons. a Representative confocal image of cultured WT ventral MB neuron axons immunolabeled with anti-GFP for transfected DAT-pHluorin (green), anti-TH (red), and anti-synapsin1/2 (blue). White arrows point to varicosities and yellow arrowheads point to boutons determined based on size (see **b**). **b** Scattered plot summarizing the size of all varicosities and the synapsin1/2 immunofluorescence of varicosities relative to boutons (see the "Methods" section). The gray box indicates the size distribution of all varicosities analyzed and the orange box indicates the empirical size of the bouton (<3.14 μm²). **c** Box plot of synapsin1/2 immunofluorescence of _n_ = 94 boutons and _n_ = 35 varicosities from three batches of cultures. ****_p_ < 0.0001, Mann–Whitney test. **d** Box plot for the number of varicosities/axon area (see the "Methods" section) in _Synj1_+/− and littermate cultures. _Synj1_+/+: _n_ = 22 images, _Synj1_+/−: _n_ = 21 images from three batches of cultures. _p_ > 0.05, Mann–Whitney test.

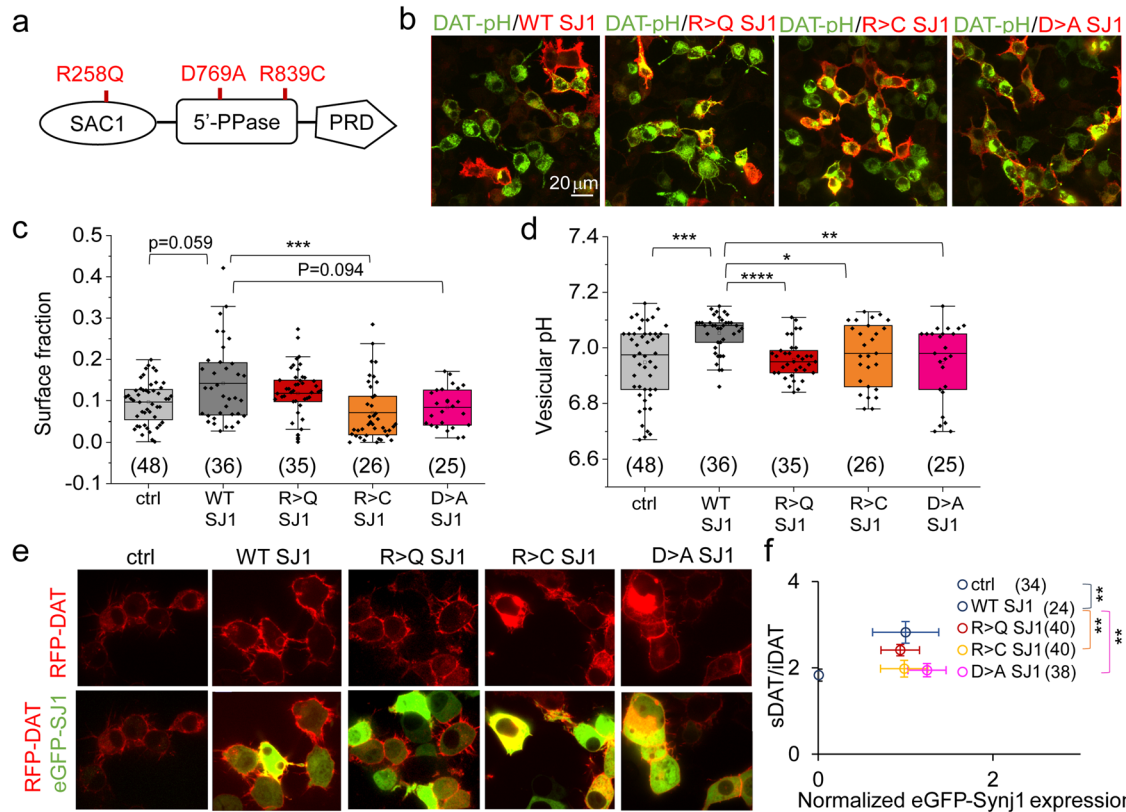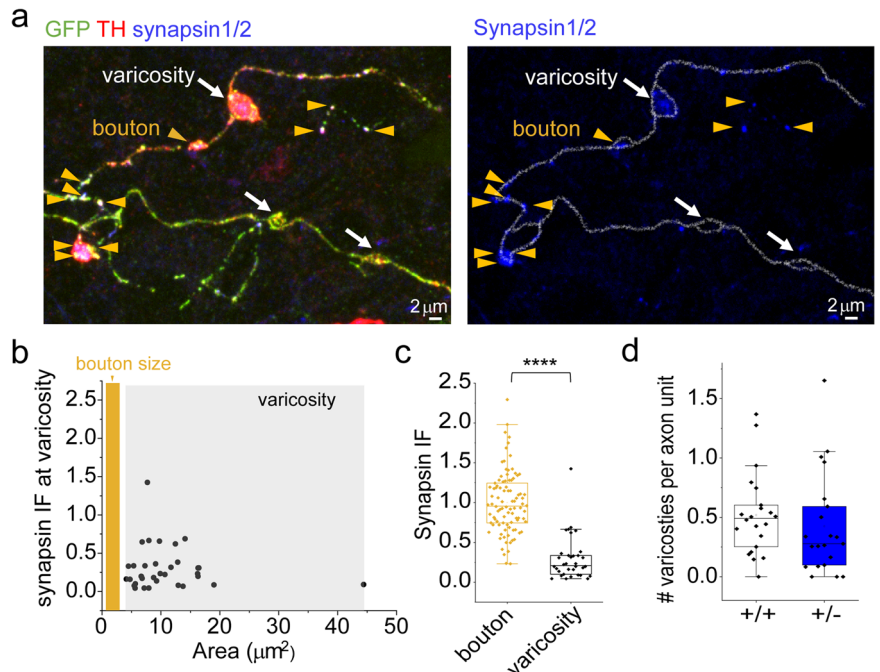**Fig. 6 | Synj1's 5′-phosphatase domain is essential for the maintenance of basal-level surface DAT. a** Synj1 domain structure and mutations examined in this study. The R258Q and R839C mutations were associated with PD. The D730A mutation completely abolishes the 5′-PPase activity. **b** Representative images of N2a cells co-transfected with DAT-pHluorin and different variants of SYNJ1 immunolabeled by anti-GFP (green) and anti-Synj1 (red). **c** and **d** Analysis of DAT surface fraction (**c**) and vesicular pH (**d**) for DAT-pHluorin expressing N2a cells. The _n_ = cell number was from three independent batches of cultures. **e** Representative images of N2a cells transfected with RFP-DAT (red) or co-transfected with RFP-DAT (red) and different variants of eGFP-SYNJ1 (green). **f** 2-dimensional distribution of surface RFP/intracellular RFP (sDAT/iDAT) and normalized GFP fluorescence for all cells. _n_ from 2 to 3 independent batches of cultures. *_p_ < 0.05, **_p_ < 0.01, ***_p_ < 0.001, ****_p_ < 0.0001. _p_ values are from Mann–Whitney tests or Dunn's post hoc tests following Kruskal–Wallis ANOVA.
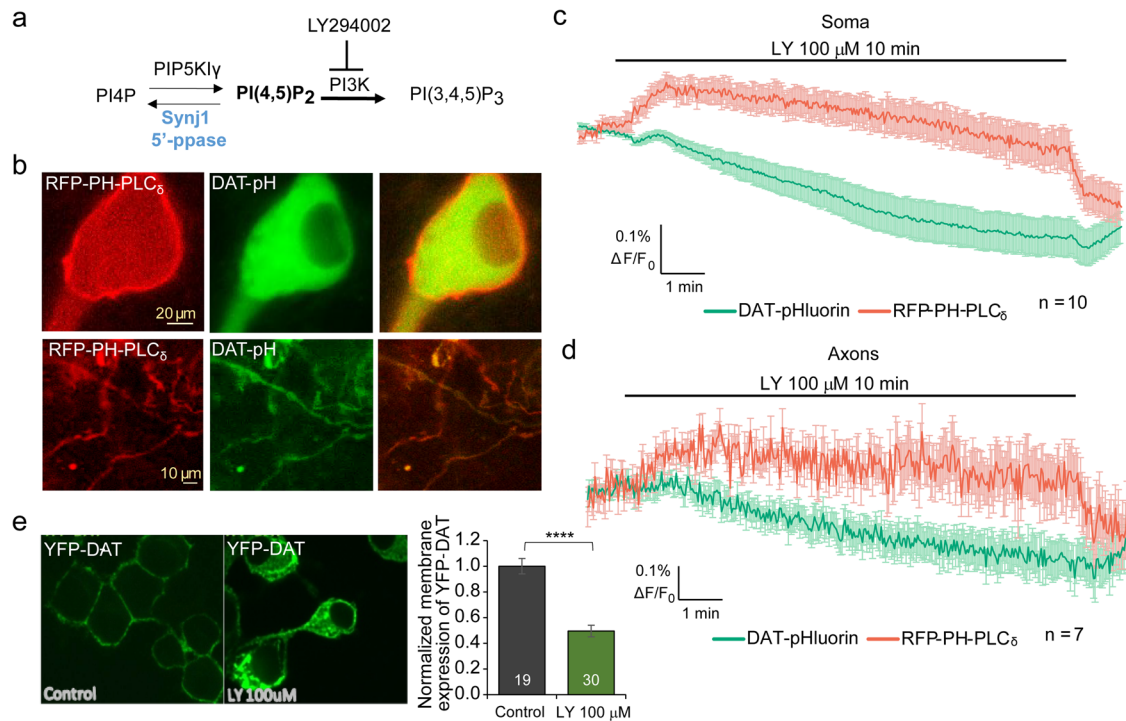
Fig. 7 | Pharmacologically increasing membrane PI(4,5)P$_2$ leads to a reduction of DAT-pHluorin fluorescence in WT neurons. a Illustration of PI(4,5)P$_2$ metabolism regulated by Synj1 and PI3K. **b** Representative images of cultured WT MB neuron soma (top) and axons (bottom) co-transfected with DAT-pHluorin and RFP-PH-PLC$_\delta$. **c** and **d** Dual channel simultaneous imaging of Soma (**c**) and axonal (**d**) DAT-pHluorin and RFP-PH-PLC$_\delta$ fluorescence when treated with a PI3K inhibitor, LY249002 (LY, 100 μM). Data = mean ± SEM. $n = 10$ for soma and $n = 7$ for axons from three batches of cultures. **e** N2a cells expressing YFP-DAT and treated with LY for 10 min. Representative images and analysis of relative surface YFP-DAT/intracellular YFP fluorescence in control and LY-treated cells. ****$p < 0.0001$, Student's t-test.

the soma and the axons (Fig. 8d, e). Collectively, we showed that increasing membrane PI(4,5)P$_2$ is sufficient to drive DAT internalization in neuronal soma and axons; and the enhanced PKCβ activity is responsible for the Synj1 deficiency-associated loss of axonal sDAT maintenance.

Discussion

Parkinson's disease (PD) is often preceded by altered dopamine (DA) signaling and loss of functional maintenance of DAergic axons[9,63,70–79]. In this study, we used the PARK20/*Synj1* haploinsufficient mouse to examine cellular and molecular mechanisms underlying Synj1 deficiency-associated DAergic dysfunction. We employed quantitative imaging approaches to demonstrate that Synj1 deficiency results in enhanced basal DA levels and altered evoked DA release kinetics. These changes are likely associated with impaired basal maintenance of surface DAT and maladaptive axonal DAT trafficking in response to extracellular DA. We showed that the baseline maintenance of sDAT is regulated through the 5'-PPase of Synj1 and its downstream PI(4,5)P$_2$–PKCβii signaling pathway. Thus, our work demonstrates a novel role of Synj1 for presynaptic trafficking and provides mechanistic insight for dysfunctional DAT regulation, which is integral to DAergic decline in PD.

In previous studies of Synj1-deficient mammalian cortical neurons, including those with complete deletion of Synj1 and those carrying the R258Q disease mutation, impaired exocytosis or neurotransmission has not been reported[15,26]. The altered DA release dynamics we show in this study, although subtle, was the first evidence that Synj1 could impact DAergic transmission. Our results corroborate our previous findings[9,25] and further underscore the DA neuron-specific vulnerability to Synj1 deficiency, which may be relevant to PD pathogenesis. Patients carrying different *SYNJ1* mutations or with reduced *SYNJ1* transcripts exhibit heterogeneous clinical manifestations and levodopa responsiveness. Although our current study does not fully address such heterogeneity, our results suggested that axonal

pathologies associated with *Synj1*+/− mice are dissimilar to the *SYNJ1* R258Q disease mutation KI mice. For example, large DAT clusters were reported in the R > Q KI mice[26], but not found in the *Synj1*+/− mice. Further, the *Synj1*+/− mutation elevates plasma membrane PI(4,5)P$_2$[9] and induces DAT internalization, while the R > Q mutation did not impact the surface fraction of the DAT likely due to the intact 5'-PPase activity[1,9]. Nonetheless, the R > Q mutation resulted in altered vesicular pH of DAT-containing endocytic vesicles in N2a cells, suggesting that DAT trafficking is disrupted in a different manner. The precise cell-autonomous pathogenic signaling among different *SYNJ1* PD mutations and their genotype–phenotype correlations are worth further investigation.

In this study, we provided evidence for the hyperactive PKCβ signaling that mediates the Synj1 deficiency-induced impairment in surface DAT maintenance. The PKCβii-induced DAT internalization at baseline could impact DA signaling, but how does the PKC-induced DAT internalization eventually contribute to DAergic decline? We have three hypotheses: (i) The increased basal DA could activate the DA D2 autoreceptor (DRD2) to inhibit DA synthesis and release[80–82]. (ii) Loss of DAT could impair its function as a Na$^+$/Cl$^−$ symporter and thus reduce the membrane excitability of DA neurons, perhaps with a stronger influence in the nigral pathway[31]. Indeed, loss-of-function mutations of DAT have been reported in patients with Parkinsonism[32–35]. (iii) If the loss of basal sDAT is a result of PKC hyperactivity, we predict a more profound change in many essential membrane transporters, receptors, and ion channels[64,65]. These trafficking defects could result in a huge burden for the intracellular degradative machinery, culminating in pathogenic inclusions and oxidative stress, characteristic of slow-progressing typical PD.

Many earlier studies showed that plasma membrane PI(4,5)P$_2$ regulates the function of a multitude of channels and transporters[83]. Direct interaction of PI(4,5)P$_2$ with the DAT or serotonin transporter (SERT) has been reported[84–86]. In many of these studies, PI(4,5)P$_2$ was suggested as an essential phospholipid in stabilizing transporter functions[84–87]. It is not
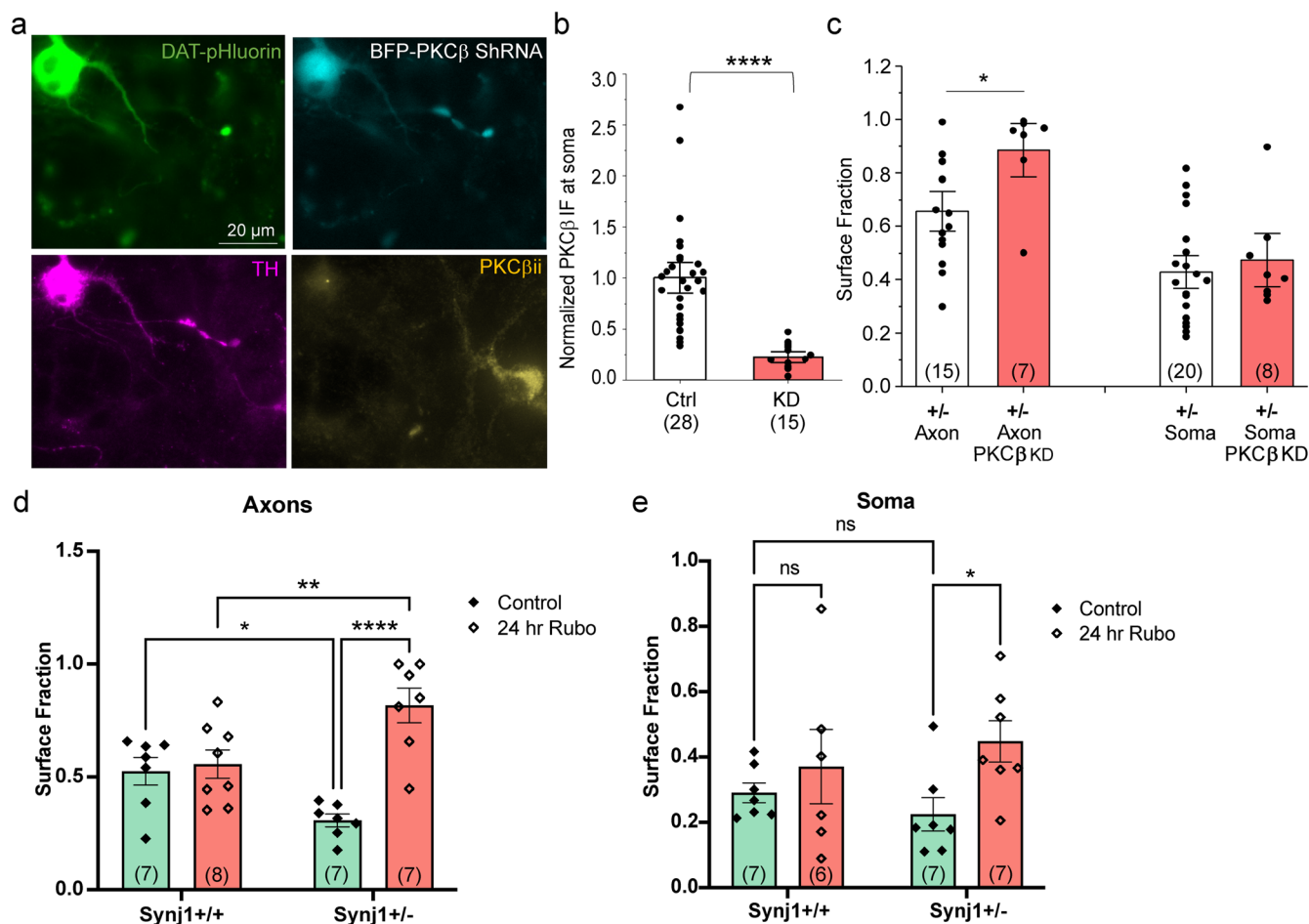
Fig. 8 | Knocking down PKCβ or inhibiting PKCβ activity restores axonal DAT surface expression in Synj1+/− neurons. a Representative image of a cultured MB neuron co-transfected with DAT-pHluorin and a BFP-tagged shRNA targeting PKCβii. Post hoc immunofluorescence for TH and PKCβii. **b** Summary of somal PKCβii immunofluorescence in control non-transfected neurons and transfected neurons expressing shRNA. ****$p < 0.0001$, Mann–Whitney test. **c** Summary of DAT surface fraction in control Synj1+/− neurons and those co-expressing DAT-pHluorin and BFP-shRNA. ****$p < 0.0001$, Mann–Whitney test. **d, e** Surface fraction analysis at the soma (**d**) and axons (**e**) for Synj1+/+ and Synj1+/− neurons in control untreated conditions or following a 24-h treatment of a PKCβ-specific inhibitor, Rubo. *$p < 0.05$, **$p < 0.01$, ***$p < 0.001$, Fisher's post hoc following Two-way ANOVA. n = number of neurons from ≥3 batches of cultures.

unlikely that the reduced sDAT in Synj1+/− neurons is a compensatory change due to the enhanced uptake activity per molecule. We showed abnormal DA clearance following phasic release (Fig. 1d, h). While this could be partly explained by the maladaptive DAT dynamics (Fig. 4f-i), it could also be contributed by transiently enhanced DAT uptake or enhanced clearance of DA by astrocytes[88–91] due to the accumulation of PI(4,5)P₂. The precise interaction between DAT trafficking and uptake function requires further investigation.

The most unexpected finding of the study is the role of Synj1 in preventing the endocytosis of the plasma membrane cargo, DAT, which is against our understanding of Synj1 as an endocytic molecule at the presynaptic terminal. The C-terminal proline-rich domain of Synj1 is recruited by membrane-bending BAR proteins, such as Endophilin and Amphiphysin, during SV endocytosis. Synj1 then cooperates with Auxilin1 (known as PARK19/DNAJC6)[92,93] to disassemble the clathrin coat for the SV. A recent proteomics study of the Auxilin−/− mice identified profound membrane sorting defects implicating DAT as well as SV proteins[63], suggesting that it is perhaps time to revisit these "endocytic" proteins for their additional roles in clathrin-dependent presynaptic sorting. Several other vacuolar protein sorting receptors, such as VPS35[94], DNAJC26 (GAK)[95], and DNAJC13 (RME-8)[96], are also implicated in monogenic Parkinsonism or PD risk. Whether and how Synj1 interacts with these sorting machinery at the DAergic terminal, and what other essential presynaptic cargos they

regulate await further investigation. Nonetheless, our study provided the first evidence that Synj1 plays pleiotropic roles to dysregulate DA signaling.

In summary, we demonstrate molecular signaling underlying an axonal trafficking defect of DAT in the Synj1+/− mice. Our work expands the current understanding of the essential gene, Synj1, in regulating neuronal function and provides essential mechanistic insight for DA neuron vulnerability in the early stage of PD.

Methods
Animals
C57BL/6J mice were purchased from the Jax lab. The Synj1+/− mouse[10] was a gift from the Pietro De Camilli laboratory at Yale University. Synj1+/− mice were crossed to the C57BL/6J mice to generate littermate pups for MB cultures. Mice were housed in the pathogen-free barrier facility at the Rutgers Robert Wood Johnson Medical School Research Tower vivarium. Handling procedures were in accordance with the National Institutes of Health guidelines approved by the Institutional Animal Care and Use Committee (IACUC). Approved IACUC protocol number: PROTO201800183.

Cell culture and transfection
Ventral MB cultures[25,97] were prepared as described previously. Ventral midbrains (containing both VTA and SN) were dissected from P0-1 mouse

pups and digested using papain (Worthington, LK003178) in a 34–37 °C water bath with gentle stirring and constant oxygenation. MB neurons were then seeded within a cloning cylinder on cover glasses pretreated with poly-L-ornithine (Sigma, P3655). Cells were plated at a density of 30,000 cells/0.28 cm^2 and grown in the Neurobasal-A-based medium supplemented with GDNF (10 ng/mL, EMD Millipore, GF030).

All transfection was performed using Lipofectamine™ 2000 (Thermo Fisher, 11668019) on DIV (days in vitro) 5–7 following a company-suggested protocol. The DNA-lipofectamine mixture was washed out after 45 min incubation at 37 °C and the growth medium was replaced with a fresh medium supplemented with an antimitotic agent, ARA-C (Sigma-Aldrich, C6645) and Glial cell-derived neurotrophic factor (GDNF, Millipore Sigma, Cat# G1777). Imaging experiments were performed between DIV 13 and DIV 17. N2a cells were cultured and passaged following an ATCC-suggested protocol using culture media containing DMEM (Thermo Fisher, 11965118), 10% fetal bovine serum (FBS) (Atlantic Biologicals, S11550), and 5% 10 U/mL Penicillin–Streptomycin (Thermo Fisher, 15140122). Cells were trypsinized using 0.05% Trypsin–EDTA (Gibco, 25300-054) and plated at 30% confluency. Transfection was carried out using Lipofectamine™ 3000 (Thermo Fisher, L3000015) following a company-suggested protocol the day after plating. The transfection mixture was left in the medium until the day of imaging (typically within 24–48 h).

Constructs
The CAGp-hDAT-pHluorin was engineered and validated as reported in our previous study[46]. The pHluorin was inserted in the second extracellular loop of human DAT. The tagRFP-C1-DAT-HA was from Addgene (#90265). The pEGFP-C1-FLAG-WT hSYNJ1-145 construct was originally gifted by Dr. Pietro De Camilli at Yale University. The pEGFP-C1-FLAG-R258Q hSYNJ1-145, pEGFP-C1-FLAG-R839C hSYNJ1-145, and pEGFP-C1-FLAG-D769A hSYNJ1-145 as well as their EGFP-deleted counterparts were generated via site-directed mutagenesis (Agilent Technology Quick-Change 200517) and reported in our previous studies[1,23,25]. The PKCβ shRNA (pRP[shRNA]-TagBFP2-U6>mPrkcb) was constructed by vector builder with a BFP tag and hairpin structure targeting mouse PKCβ: GAGATTCAGCCACCTTATAAA.

dLight1.3b sniffer cell co-culture
Dlight1.3 sniffer cells were thawed and prepared as previously described[47]. Cells were maintained in a selection medium containing 90% DMEM (Thermo Fisher #11965092), 10% fetal bovine serum (Atlanta Biologicals #S11550H), 1% Pen/Strep (Thermo Fisher #15140122), 15 µg/mL Blasticidin (Millipore Sigma, Cat# 15205) + 200 µg/mL Hygromycin (Millipore Sigma, Cat# H3274). For co-culture with the ventral MB neurons, an 8 × 8 mm cloning cylinder was placed on the MB culture at DIV 13 and filled with neuronal medium. Sniffer cells were seeded at 20,000/cylinder after trypsinization. Doxycycline (1 µg/mL) was added to the co-culture the next day for 24 h and imaging experiments were performed on DIV 15. Perfusion of different concentrations of DA solutions was carried out similarly as described in the *DAT-pHluorin imaging* section. Field electrical stimulation was delivered in a time frame-locked manner via a custom-built stimulation chamber with two platinum electrodes at 10 V/cm by the A310 Accupulser and A385 stimulus isolator (World Precision Instruments)[97,98]. A 1 ms pulse was used to evoke single-action potentials. Images were acquired at 4 Hz.

JHC dye live staining
Staining was performed following previously published protocols[55,56]. Briefly, MB cultures were washed three times in cold JHC buffer containing 25 mM HEPES, pH 7.4, with 130 mM NaCl, 5.4 mM KCl, 1.2 mM CaCl$_2$, 1.2 mM MgSO$_4$, and 5 mM D-glucose. Cell culture was then incubated with 50 nM JHC1-64 dye diluted in JHC buffer containing 1 mM L-ascorbic acid, at 4 °C to avoid internalization for 30 minutes. For negative control, 10 µM

cocaine was included in the JHC buffer. After incubation, the dye was washed away three times with ice-cold JHC buffer, followed by immediate fixation with 4% PFA at room temperature. Images were taken immediately using confocal microscopy.

DAT-pHluorin live imaging
For live cell imaging, cells on cover glass were mounted on a custom-made laminar-flow chamber with constant gravity perfusion (at a rate of ~0.2–0.3 mL/min) of a Tyrode's salt solution containing 119 mM NaCl, 2.5 mM KCl, 2 mM CaCl$_2$, 2 mM MgCl$_2$, 25 mM HEPES, 30 mM glucose, 10 µM 6-cyano-7-nitroquinoxaline-2,3-dione (CNQX), and 50 µM D, L-2-amino-5-phosphonovaleric acid (AP-5) and buffered to pH 7.40. The NH$_4$Cl medium contains 50 mM NH$_4$Cl, 70 mM NaCl, 2.5 mM KCl, 2 mM CaCl$_2$, 2 mM MgCl$_2$, 25 mM HEPES, 30 mM Glucose, 10 µM CNQX, and 50 µM AP-5, buffered to pH 7.40. The MES medium contains 25 mM MES, 70 mM NaCl, 2.5 mM KCl, 2 mM CaCl$_2$, 2 mM MgCl$_2$, 30 mM Glucose, 10 µM CNQX, and 50 µM AP-5, buffered to pH 5.50. Perfusion of Tyrode's solution, as well as pharmacological reagents (DA hydrochloride and LY294002) buffered in Tyrode's solution, is regulated by Valvelink 8.2 and the NH$_4$Cl or MES solutions were perfused by pipettes. All chemicals were purchased from Sigma-Aldrich or Tocris Bioscience unless otherwise noted. For the overnight Ruboxistaurin treatment study, Ventral MB cultures transfected with DAT-pHluorin were treated with 1 µM Ruboxistaurin (Rubo, LY333531) HCl (Selleck Chemicals, Cat #S7663) diluted in the culture media on DIV 15–16 for at least 18 h not to exceed 24 h prior to live imaging using MES–NH$_4$Cl to measure the surface fraction of DAT. Temperature was clamped at ~31.0 °C at the objective throughout the experiment. Images were acquired using a highly sensitive, back-illuminated EM-CCD camera (iXon+ Model DU-897E-BV, Andor Corp., CT, USA). Nikon Ti-2 wide-field microscope is modified with Spectra-X (Lumencor) as the light source for shuttered illumination. pHluorin fluorescence excitation and collection were using a Nikon PLan APO ×60 1.40 NA objective using 525/50 m emission filter and 495LP dichroic filters (Chroma, 49002).

Western blots
Brain samples were lysed using a Triton-based lysis buffer containing 50 mM Tris–HCl (pH 7.5), 150 mM NaCl, and 1% Triton as well as protease and phosphatase inhibitors as previously described[9,23,25]. After centrifugation at 16,000 × g, 4 °C for 30 min, the supernatant was collected for protein quantification using the Pierce BCA assay (Thermo 23227). Typically, 10–20 µg of total proteins were loaded for each sample on the Invitrogen 4–12% Bis–Tris gel and transferred to a PVDF membrane (Thermo 88518). Pellet was washed in PBST (1% Triton) three times, solubilize in 2% SDS at 60 C for an hour, followed by centrifugation at 15,000 × g for 20 min. Supernatant is collected and analyzed on the Bis–Tris gel as the insoluble fraction.

Amphetamine analysis
Mice were brought to the behavioral room 1 h before the test started. Each mouse was gently placed in the center of a clean 19 × 19-inch cage with a Versamax monitor system (Accuscan). After a 30-min free exploration, the mouse was subject to intraperitoneal injection following a standard procedure. The mouse was appropriately restrained, and a sterile and new needle was inserted bevel-side up into the lower right quadrant of the peritoneal cavity. 5 mg/kg sterile amphetamine (0.2–0.5 µL, Sigma A5880) was injected into each mouse before placing it back in the center of the cage for continued monitoring for an additional 40 min. Data was binned at 5-min intervals and processed by the Fusion software.

Immunohistochemistry
Mice were anesthetized using the isoflurane drop method, perfused trans-cardially with 4% fresh paraformaldehyde, and post-fixed with 4% paraformaldehyde for over two hours. Dissected brains were cryoprotected in 30% sucrose prior to flash-freezing in the OCT-compound media (SAKURA). Coronal sections were sliced at 40 µm thickness on a Leica CM 3050S research cryostat and kept at an anti-freeze medium for

immunohistolochemical (IHC) analysis. IHC was carried out following a standard protocol as previously described[9]. Briefly, tissue slices were washed in 1X PBS and blocked in 5% goat serum for 30–60 min. Primary antibodies diluted in 5% goat serum were applied and incubated overnight at 4 °C, followed by Alexa Fluor® secondary antibodies (Invitrogen™). The tissue slices were then subjected to extended washing using 1X PBS to reduce background fluorescence before mounting with Diamond Antifade Mountant (Thermo Fisher Scientific, P36962). Immunofluorescence was analyzed using a Nikon CREST spinning disk confocal microscope. 3–5 regions per brain slice were selected randomly for imaging, and 2–3 slices per mouse were used for analysis. The same imaging parameters were set for each batch of culture. Image stacks were taken at different focal planes at 0.9 μm intervals, and a maximum projection image was generated for each stack via ImageJ for analysis.

Post hoc analysis for live imaging experiments
Stages of interest were recorded during live imaging using Nikon Instruments Elements acquisition software. First, set reference stage 0 at the left side of the imaging field. Multiple easy-to-identify structures were typically recorded to provide an estimate of $x-y$ offset during post hoc analysis. Following the live experiments, neuronal cultures or cocultures were immediately fixed in 4% PFA and followed by immunocytochemistry as detailed above. An anti-GFP antibody is typically used along with others to find DAT-pHluroin or sniffer cells. Coverslips were mounted in the same orientation as the live imaging session to ensure accurate stage positions. After locating the stage to the reference stage 0 position, use the reset function to recalibrate the recorded stages and to find the neuronal soma, axons, or sniffer cells that match the live imaging experiment (see examples in Fig. 1a, Supplementary Fig. 2, Fig. 8a).

Antibodies
The following primary antibodies were used for IHC: rat anti-DAT (EMD Millipore, MAB369, RRID AB_2190413, 1:1000 dilution), rabbit anti-synj1 (Novus Biologicals, NBP1-87842, RRID: AB_11047653,1:500 dilution). Antibodies used for western blots: rabbit anti-DAT (Millipore-Sigma, AB2231, RRID: AB_1586991,1:1000), mouse anti-DAT (Thermo Fisher, MA524796, RRID: AB_2717269, 1:1000), mouse anti-β-actin (Cell Signaling, 3700, RRID: AB_2242334, 1:1000). Antibodies used for immunocytochemistry: rat anti-DAT (EMD Millipore, MAB369, RRID: AB_2190413, 1:1000 dilution), guinea pig anti-synapsin 1/2 (Synaptic System, 106004, RRID: AB_1106784, 1:500 dilution), chicken anti-GFP (Thermo Fisher, A-10262, RRID: AB_2534023, 1:1000), rabbit anti-TH (Novus Biologicals, NB300-109, RRID: AB_350437, 1:1000), mouse anti-TH (Sigma, T2928, RRID: AB_477569, 1:1000), rabbit anti-synj1 (Novus Biologicals, NBP1-87842, RRID: AB_11047653, 1:500), mouse anti-PKCα (Novus Biologicals, NB600-201SS, RRID: AB_10003372, 1:1000), mouse anti-PKCβii(F-7) (Santa Cruz, sc-13149, RRID: AB_628144, 1:50), and pSer660 PKCβ (Cell Signaling, #9371, RRID: AB_2168219, 1:1000).

Varicosity analysis
Confocal stacks of fixed and immunolabeled cells were captured at 0.5 μm steps and projected by maximum intensity. Varicosity size was determined by tracing large TH+ structures using the freehand tool in ImageJ. Bouton size was determined by placing 2 × 2 μm circular regions of interests (ROIs) using the Time Series Analyzer plugin. All synapsin1/2 immunolabeled puncta in our analysis can be placed within the 2 × 2 μm circular ROIs, therefore, we empirically determined the bouton size to be 0–3.14 μm². The total axon area for each image was determined by generating a binary image for synapsin1/2 immunofluorescence channel. The total pixel area for synapsin1/2 was used as a proxy for axon area to determine the density of large varicosities in the imaging field.

Data analysis and statistics
DAT-pHluorin surface fraction was calculated as detailed in our previous publication[46]. All images were analyzed using ImageJ or FIJI. Measurements of axon or surface fluorescence were obtained using the segmented line function. Measurements of soma or intracellular fluorescence were obtained using the freehand selections. All data was subject to a normality test. Student's t-test, One-way ANOVA, or Two-way ANOVA were used only if all datasets were normally distributed. If one or more datasets did not conform to a normal distribution, the Mann–Whitney test or Kruskal–Wallis ANOVA was used. All western blots had over two technical repeats, and all cell culture analyses were from 2 to 6 independent cultures.

Data availability
All data generated are included in this article and its Supplementary Information. Additional minimal dataset necessary to interpret, replicate and build upon the methods or findings reported in the article data will be provided upon request.

References
1. Krebs, C. E. et al. The Sac1 domain of SYNJ1 identified mutated in a family with early-onset progressive Parkinsonism with generalized seizures. *Hum. Mutat.* **34**, 1200–1207 (2013).
2. Quadri, M. et al. Mutation in the SYNJ1 gene associated with autosomal recessive, early-onset Parkinsonism. *Hum. Mutat.* **34**, 1208–1215 (2013).
3. Olgiati, S. et al. PARK20 caused by SYNJ1 homozygous Arg258Gln mutation in a new Italian family. *Neurogenetics* **15**, 183–188 (2014).
4. Kirola, L. et al. Identification of a novel homozygous mutation Arg459Pro in SYNJ1 gene of an Indian family with autosomal recessive juvenile Parkinsonism. *Parkinsonism Relat. Disord.* **31**, 124–128 (2016).
5. Rauschendorf, M. A. et al. Novel compound heterozygous synaptojanin-1 mutation causes L-DOPA-responsive dystonia-Parkinsonism syndrome. *Mov. Disord.* **32**, 478–480 (2017).
6. Taghavi, S. et al. A clinical and molecular genetic study of 50 families with autosomal recessive Parkinsonism revealed known and novel gene mutations. *Mol. Neurobiol.* **55**, 3477–3489 (2018).
7. Xie, F. et al. A novel homozygous SYNJ1 mutation in two siblings with typical Parkinson's disease. *Parkinsonism Relat. Disord.* **69**, 134–137 (2019).
8. Lesage, S. et al. Clinical variability of SYNJ1-associated early-onset Parkinsonism. *Front. Neurol.* **12**, 648457 (2021).
9. Pan, P. Y. et al. Synj1 haploinsufficiency causes dopamine neuron vulnerability and alpha-synuclein accumulation in mice. *Hum. Mol. Genet.* **29**, 2300–2312 (2020).
10. Cremona, O. et al. Essential role of phosphoinositide metabolism in synaptic vesicle recycling. *Cell* **99**, 179–188 (1999).
11. McPherson, P. S. et al. A presynaptic inositol-5-phosphatase. *Nature* **379**, 353–357 (1996).
12. Di Paolo, G. & De Camilli, P. Phosphoinositides in cell regulation and membrane dynamics. *Nature* **443**, 651–657 (2006).
13. Choudhry, H., Aggarwal, M. & Pan, P. Y. Mini-review: synaptojanin 1 and its implications in membrane trafficking. *Neurosci. Lett.* **765**, 136288 (2021).
14. Verstreken, P. et al. Synaptojanin is recruited by endophilin to promote synaptic vesicle uncoating. *Neuron* **40**, 733–748 (2003).
15. Mani, M. et al. The dual phosphatase activity of synaptojanin1 is required for both efficient synaptic vesicle endocytosis and reavailability at nerve terminals. *Neuron* **56**, 1004–1018 (2007).
16. Milosevic, I. et al. Recruitment of endophilin to clathrin-coated pit necks is required for efficient vesicle uncoating after fission. *Neuron* **72**, 587–601 (2011).
17. Chang-Ileto, B. et al. Synaptojanin 1-mediated PI(4,5)P2 hydrolysis is modulated by membrane curvature and facilitates membrane fission. *Dev. Cell* **20**, 206–218 (2011).

18. Dong, Y. et al. Synaptojanin cooperates in vivo with endophilin through an unexpected mechanism. *Elife* **4**, e05660 (2015).
19. Watanabe, S. et al. Synaptojanin and endophilin mediate neck formation during ultrafast endocytosis. *Neuron* **98**, 1184–1197 e6 (2018).
20. Saheki, Y. & De Camilli, P. Synaptic vesicle endocytosis. *Cold Spring Harb. Perspect. Biol.* **4**, a005645 (2012).
21. Luthi, A. et al. Synaptojanin 1 contributes to maintaining the stability of GABAergic transmission in primary cultures of cortical neurons. *J. Neurosci.* **21**, 9101–9111 (2001).
22. Vanhauwaert, R. et al. The SAC1 domain in synaptojanin is required for autophagosome maturation at presynaptic terminals. *EMBO J.* **36**, 1392–1411 (2017).
23. Pan, P. Y. et al. Synaptojanin1 deficiency upregulates basal autophagosome formation in astrocytes. *J. Biol. Chem.* **297**, 100873 (2021).
24. Yang, S. et al. Presynaptic autophagy is coupled to the synaptic vesicle cycle via ATG-9. *Neuron* **110**, 824–840.e10 (2022).
25. Pan, P. Y. et al. Parkinson's disease-associated LRRK2 hyperactive kinase mutant disrupts synaptic vesicle trafficking in ventral midbrain neurons. *J. Neurosci.* **37**, 11366–11376 (2017).
26. Cao, M. et al. Parkinson Sac domain mutation in Synaptojanin 1 impairs clathrin uncoating at synapses and triggers dystrophic changes in dopaminergic axons. *Neuron* **93**, 882–896.e5 (2017).
27. Nirenberg, M. J. et al. The dopamine transporter is localized to dendritic and axonal plasma membranes of nigrostriatal dopaminergic neurons. *J. Neurosci.* **16**, 436–447 (1996).
28. Hersch, S. M. et al. Subcellular localization and molecular topology of the dopamine transporter in the striatum and substantia nigra. *J. Comp. Neurol.* **388**, 211–227 (1997).
29. Jaber, M. et al. The dopamine transporter: a crucial component regulating dopamine transmission. *Mov. Disord.* **12**, 629–633 (1997).
30. Ingram, S. L., Prasad, B. M. & Amara, S. G. Dopamine transporter-mediated conductances increase excitability of midbrain dopamine neurons. *Nat. Neurosci.* **5**, 971–978 (2002).
31. Condon, M. D. et al. Plasticity in striatal dopamine release is governed by release-independent depression and the dopamine transporter. *Nat. Commun.* **10**, 4263 (2019).
32. Hansen, F. H. et al. Missense dopamine transporter mutations associate with adult Parkinsonism and ADHD. *J. Clin. Investig.* **124**, 3107–3120 (2014).
33. Herborg, F. et al. Identifying dominant-negative actions of a dopamine transporter variant in patients with Parkinsonism and neuropsychiatric disease. *JCI Insight* **6**, e151496 (2021).
34. Kurian, M. A. et al. Homozygous loss-of-function mutations in the gene encoding the dopamine transporter are associated with infantile Parkinsonism-dystonia. *J. Clin. Investig.* **119**, 1595–1603 (2009).
35. Ng, J. et al. Dopamine transporter deficiency syndrome: phenotypic spectrum from infancy to adulthood. *Brain* **137**, 1107–1119 (2014).
36. Daniels, G. M. & Amara, S. G. Regulated trafficking of the human dopamine transporter. Clathrin-mediated internalization and lysosomal degradation in response to phorbol esters. *J. Biol. Chem.* **274**, 35794–35801 (1999).
37. Zahniser, N. R. & Sorkin, A. Trafficking of dopamine transporters in psychostimulant actions. *Semin. Cell Dev. Biol.* **20**, 411–417 (2009).
38. Block, E. R. et al. Brain region-specific trafficking of the dopamine transporter. *J. Neurosci.* **35**, 12845–12858 (2015).
39. Lee, F. J. et al. Dopamine transporter cell surface localization facilitated by a direct interaction with the dopamine D2 receptor. *EMBO J.* **26**, 2127–2136 (2007).
40. Li, L. B. et al. The role of N-glycosylation in function and surface trafficking of the human dopamine transporter. *J. Biol. Chem.* **279**, 21012–21020 (2004).
41. Sorkina, T. et al. Constitutive and protein kinase C-induced internalization of the dopamine transporter is mediated by a clathrin-dependent mechanism. *Traffic* **6**, 157–170 (2005).
42. Wu, S. et al. The dopamine transporter recycles via a retromer-dependent postendocytic mechanism: tracking studies using a novel fluorophore-coupling approach. *J. Neurosci.* **37**, 9438–9452 (2017).
43. Bu, M., Farrer, M. J. & Khoshbouei, H. Dynamic control of the dopamine transporter in neurotransmission and homeostasis. *NPJ Parkinsons Dis.* **7**, 22 (2021).
44. Fagan, R. R., Kearney, P. J. & Melikian, H. E. In situ regulated dopamine transporter trafficking: there's no place like home. *Neurochem. Res.* **45**, 1335–1343 (2020).
45. Wheeler, D. S. et al. Amphetamine activates Rho GTPase signaling to mediate dopamine transporter internalization and acute behavioral effects of amphetamine. *Proc. Natl Acad. Sci. USA* **112**, E7138–E7147 (2015).
46. Saenz, J. et al. Cocaine-regulated trafficking of dopamine transporters in cultured neurons revealed by a pH sensitive reporter. *iScience* **26**, 105782 (2023).
47. Klein Herenbrink, C. et al. Multimodal detection of dopamine by sniffer cells expressing genetically encoded fluorescent sensors. *Commun. Biol.* **5**, 578 (2022).
48. Patriarchi, T. et al. Ultrafast neuronal imaging of dopamine dynamics with designed genetically encoded sensors. *Science* **360**, eaat4422 (2018).
49. Dagra, A. et al. alpha-Synuclein-induced dysregulation of neuronal activity contributes to murine dopamine neuron vulnerability. *NPJ Parkinsons Dis.* **7**, 76 (2021).
50. Stoier, J. F. et al. Amphetamine-induced reverse transport of dopamine does not require cytosolic Ca(2). *J. Biol. Chem.* **299**, 105063 (2023).
51. Ji, J. & Dluzen, D. E. Sex differences in striatal dopaminergic function within heterozygous mutant dopamine transporter knock-out mice. *J. Neural Transm. (Vienna)* **115**, 809–17 (2008).
52. Bhatt, S. D. & Dluzen, D. E. Dopamine transporter function differences between male and female CD-1 mice. *Brain Res.* **1035**, 188–195 (2005).
53. Zachry, J. E. et al. Sex differences in dopamine release regulation in the striatum. *Neuropsychopharmacology* **46**, 491–499 (2021).
54. Cha, J. H. et al. Rhodamine-labeled 2beta-carbomethoxy-3beta-(3,4-dichlorophenyl)tropane analogues as high-affinity fluorescent probes for the dopamine transporter. *J. Med. Chem.* **48**, 7513–7516 (2005).
55. Eriksen, J. et al. Visualization of dopamine transporter trafficking in live neurons by use of fluorescent cocaine analogs. *J. Neurosci.* **29**, 6794–6808 (2009).
56. Guthrie, D. A. et al. Novel fluorescent ligands enable single-molecule localization microscopy of the dopamine transporter. *ACS Chem. Neurosci.* **11**, 3288–3300 (2020).
57. Ashrafi, G. et al. GLUT4 mobilization supports energetic demands of active synapses. *Neuron* **93**, 606–615.e3 (2017).
58. Miesenbock, G., De Angelis, D. A. & Rothman, J. E. Visualizing secretion and synaptic transmission with pH-sensitive green fluorescent proteins. *Nature* **394**, 192–195 (1998).
59. Sankaranarayanan, S. et al. The use of pHluorins for optical measurements of presynaptic activity. *Biophys. J.* **79**, 2199–2208 (2000).
60. Salahpour, A. et al. Increased amphetamine-induced hyperactivity and reward in mice overexpressing the dopamine transporter. *Proc. Natl Acad. Sci. USA* **105**, 4405–4410 (2008).
61. Fibiger, H. C., Fibiger, H. P. & Zis, A. P. Attenuation of amphetamine-induced motor stimulation and stereotypy by 6-hydroxydopamine in the rat. *Br. J. Pharm.* **47**, 683–692 (1973).
62. Ng, X. Y. et al. Mutations in Parkinsonism-linked endocytic proteins synaptojanin1 and auxilin have synergistic effects on dopaminergic axonal pathology. *NPJ Parkinsons Dis.* **9**, 26 (2023).
63. Vidyadhara, D. J. et al. Dopamine transporter and synaptic vesicle sorting defects underlie auxilin-associated Parkinson's disease. *Cell Rep.* **42**, 112231 (2023).

64. Antal, C. E. & Newton, A. C. Tuning the signalling output of protein kinase C. *Biochem. Soc. Trans.* **42**, 1477–1483 (2014).
65. Steinberg, S. F. Structural basis of protein kinase C isoform function. *Physiol. Rev.* **88**, 1341–1378 (2008).
66. Loder, M. K. & Melikian, H. E. The dopamine transporter constitutively internalizes and recycles in a protein kinase C-regulated manner in stably transfected PC12 cell lines. *J. Biol. Chem.* **278**, 22168–22174 (2003).
67. Miranda, M. et al. Enhanced ubiquitylation and accelerated degradation of the dopamine transporter mediated by protein kinase C. *J. Biol. Chem.* **280**, 35617–35624 (2005).
68. Cremona, M. L. et al. Flotillin-1 is essential for PKC-triggered endocytosis and membrane microdomain localization of DAT. *Nat. Neurosci.* **14**, 469–477 (2011).
69. Keranen, L. M., Dutil, E. M. & Newton, A. C. Protein kinase C is regulated in vivo by three functionally distinct phosphorylations. *Curr. Biol.* **5**, 1394–1403 (1995).
70. Richfield, E. K. et al. Behavioral and neurochemical effects of wild-type and mutated human alpha-synuclein in transgenic mice. *Exp. Neurol.* **175**, 35–48 (2002).
71. Itier, J. M. et al. Parkin gene inactivation alters behaviour and dopamine neurotransmission in the mouse. *Hum. Mol. Genet.* **12**, 2277–2291 (2003).
72. Kim, R. H. et al. Hypersensitivity of DJ-1-deficient mice to 1-methyl-4-phenyl-1,2,3,6-tetrahydropyrindine (MPTP) and oxidative stress. *Proc. Natl Acad. Sci. USA* **102**, 5215–5220 (2005).
73. Fleming, S. M. et al. Behavioral effects of dopaminergic agonists in transgenic mice overexpressing human wildtype alpha-synuclein. *Neuroscience* **142**, 1245–1253 (2006).
74. Tong, Y. et al. R1441C mutation in LRRK2 impairs dopaminergic neurotransmission in mice. *Proc. Natl Acad. Sci. USA* **106**, 14622–14627 (2009).
75. Melrose, H. L. et al. Impaired dopaminergic neurotransmission and microtubule-associated protein tau alterations in human LRRK2 transgenic mice. *Neurobiol. Dis.* **40**, 503–517 (2010).
76. Janezic, S. et al. Deficits in dopaminergic transmission precede neuron loss and dysfunction in a new Parkinson model. *Proc. Natl Acad. Sci. USA* **110**, E4016–E4025 (2013).
77. Longo, F. et al. Age-dependent dopamine transporter dysfunction and Serine129 phospho-alpha-synuclein overload in G2019S LRRK2 mice. *Acta Neuropathol. Commun.* **5**, 22 (2017).
78. Cataldi, S. et al. Altered dopamine release and monoamine transporters in Vps35 p.D620N knock-in mice. *NPJ Parkinsons Dis.* **4**, 27 (2018).
79. Cramb, K. M. L. et al. Impaired dopamine release in Parkinson's disease. *Brain* **146**, 3117–3132 (2023).
80. Civelli, O., Bunzow, J. R. & Grandy, D. K. Molecular diversity of the dopamine receptors. *Annu. Rev. Pharm. Toxicol.* **33**, 281–307 (1993).
81. Ford, C. P. The role of D2-autoreceptors in regulating dopamine neuron activity and transmission. *Neuroscience* **282**, 13–22 (2014).
82. Tang, L., Todd, R. D. & O'Malley, K. L. Dopamine D2 and D3 receptors inhibit dopamine release. *J. Pharm. Exp. Ther.* **270**, 475–479 (1994).
83. Suh, B. C. & Hille, B. PIP2 is a necessary cofactor for ion channel function: how and why? *Annu. Rev. Biophys.* **37**, 175–195 (2008).
84. Belovich, A. N. et al. A network of phosphatidylinositol (4,5)-bisphosphate (PIP(2)) binding sites on the dopamine transporter regulates amphetamine behavior in *Drosophila melanogaster*. *Mol. Psychiatry* **26**, 4417–4430 (2021).
85. Buchmayer, F. et al. Amphetamine actions at the serotonin transporter rely on the availability of phosphatidylinositol-4,5-bisphosphate. *Proc. Natl Acad. Sci. USA* **110**, 11642–11647 (2013).
86. Hamilton, P. J. et al. PIP2 regulates psychostimulant behaviors through its interaction with a membrane protein. *Nat. Chem. Biol.* **10**, 582–589 (2014).
87. Luethi, D. et al. Phosphatidylinositol 4,5-bisphosphate (PIP(2)) facilitates norepinephrine transporter dimerization and modulates substrate efflux. *Commun. Biol.* **5**, 1259 (2022).
88. Petrelli, F. et al. Dysfunction of homeostatic control of dopamine by astrocytes in the developing prefrontal cortex leads to cognitive impairments. *Mol. Psychiatry* **25**, 732–749 (2020).
89. Chemuturi, N. V. & Donovan, M. D. Role of organic cation transporters in dopamine uptake across olfactory and nasal respiratory tissues. *Mol. Pharm.* **4**, 936–942 (2007).
90. Gasser, P. J. Roles for the uptake(2) transporter OCT3 in regulation of dopaminergic neurotransmission and behavior. *Neurochem. Int.* **123**, 46–49 (2019).
91. Dahlin, A. et al. Expression and immunolocalization of the plasma membrane monoamine transporter in the brain. *Neuroscience* **146**, 1193–1211 (2007).
92. Olgiati, S. et al. DNAJC6 mutations associated with early-onset Parkinson's disease. *Ann. Neurol.* **79**, 244–256 (2016).
93. Edvardson, S. et al. A deleterious mutation in DNAJC6 encoding the neuronal-specific clathrin-uncoating co-chaperone auxilin, is associated with juvenile Parkinsonism. *PLoS ONE* **7**, e36458 (2012).
94. Williams, E. T., Chen, X. & Moore, D. J. VPS35, the retromer complex and Parkinson's disease. *J. Parkinsons Dis.* **7**, 219–233 (2017).
95. Li, C. et al. Mutation analysis of DNAJC family for early-onset Parkinson's disease in a Chinese cohort. *Mov. Disord.* **35**, 2068–2076 (2020).
96. Vilarino-Guell, C. et al. DNAJC13 mutations in Parkinson disease. *Hum. Mol. Genet.* **23**, 1794–1801 (2014).
97. Pan, P. Y. & Ryan, T. A. Calbindin controls release probability in ventral tegmental area dopamine neurons. *Nat. Neurosci.* **15**, 813–815 (2012).
98. Pan, P. Y., Marrs, J. & Ryan, T. A. Vesicular glutamate transporter 1 orchestrates recruitment of other synaptic vesicle cargo proteins during synaptic vesicle recycling. *J. Biol. Chem.* **290**, 22593–22601 (2015).

Author contributions
J.S. and P.-Y.P. conceptualized the project, collected data, and performed data analysis. E.K. contributed to the PKC knockdown study, M.A. contributed to DAT western blot analysis and early stage of the investigation, A.S. contributed to DAT and PKC expression analysis, R.G. contributed to DAT immunofluorescence study. F.H. contributed to establishing the sniffer cells and the coculture system. P.-Y.P. wrote the manuscript. P.-Y.P., J.S. and F.H. edited the manuscript. P.-Y.P. obtained funding.

Competing interests
The authors declare no competing interests.

Additional information
Supplementary information The online version contains supplementary material available at https://doi.org/10.1038/s41531-024-00769-0.

Correspondence and requests for materials should be addressed to Ping-Yue Pan.

Reprints and permissions information is available at http://www.nature.com/reprints

Publisher's note Springer Nature remains neutral with regard to jurisdictional claims in published maps and institutional affiliations.